Ocean Modelling 68 (2013) 72–87

Contents lists available at SciVerse ScienceDirect

Ocean Modelling

journal homepage: www.elsevier.com/locate/ocemod

Numerical modelling of wave current interactions at a local scale

Maria João Teles [a,*], António A. Pires-Silva [a], Michel Benoit [b]

[a] Instituto Superior Técnico, ULisbon, Av. Rovisco Pais, 1049-001 Lisboa, Portugal
[b] Saint-Venant Laboratory for Hydraulics, Université Paris-Est (joint research unit between EDF R&D, CETMEF, and Ecole des Ponts ParisTech), 6 quai Watier, BP 49, 78401 Chatou, France

ARTICLE INFO

Article history:
Received 18 August 2012
Received in revised form 11 April 2013
Accepted 19 April 2013
Available online 9 May 2013

Keywords:
Wave–current interaction
CFD RANS solver
Code_Saturne

ABSTRACT

The present work is focused on the evaluation of wave–current interactions through numerical simulations of combined wave and current flows with the *Code_Saturne* (Archambeau et al., 2004), an advanced CFD solver based on the RANS (Reynolds Averaged Navier–Stokes) equations. The objectives of this paper are twofold. Firstly, changes in the mean horizontal velocity and the horizontal-velocity amplitude profiles are studied when waves are superposed on currents. The influence of various first and second order turbulence closure models is addressed. The results of the numerical simulations are compared to the experimental data of Klopman (1994) and Umeyama (2005). Secondly, a more detailed study of the shear stresses and the turbulence viscosity vertical profile changes is also pursued when waves and currents interact. This analysis is completed using the data from Umeyama (2005). A relationship between a non-dimensional parameter involving the turbulence viscosity and the Ursell number is subsequently proposed.

1. Introduction

The coastal environment is a complex system in which distinct physical processes with different temporal and spatial scales interact. The design of coastal protection and harbour structures, the evaluation of sediment transport and coastal erosion, the assessment of wave power potential or the impact of a park of wave energy devices are examples of possible applications that can benefit from an enhanced knowledge of these phenomena.

The combined effects of waves and currents in free surface flows have been the subject of many studies due to their impacts on coastal hydrodynamics. In this environment, horizontal and vertical velocities, as well as shear stresses, depend strongly on the interactions of waves and currents. The vertical profiles of these variables are modified and these are major issues in near-shore waves and currents modelling. Some experiments have been designed to evaluate these modifications. The experiments were initially driven by the motivation to understand how these interactions affect the bottom boundary layer and the near bed shear stresses, which may have consequences on sediment transport. Therefore, these experiments were focused on the bottom boundary layer.

Kemp and Simons (1982, 1983) carried out laboratory experiments in a flume with rough and smooth beds, and with waves following and opposing currents, over the entire depth. They observed that when waves were following the current, the mean horizontal velocity reached a maximum value at a level between the bottom boundary layer and the wave trough. On the other hand, when waves were opposing the current, the mean horizontal velocity reached a maximum at the free surface which is higher than the value observed with the logarithmic profile for a only current case. The reader is also referred to the references therein for a discussion of previous experiments. Similar results were obtained by Klopman (1994) in a series of experiments in a wave flume with a rough bed. His measurements included both the mean horizontal velocity and the horizontal-velocity amplitude for regular and irregular waves with (i) waves opposing currents, (ii) waves following currents, (iii) only waves, and (iv) only currents. In the case of only currents, more detailed observations were made, including shear and normal stresses. The observed velocity shear is in agreement with the conclusions of Kemp and Simons (1982, 1983). Klopman (1994) also reported a reduction in the near-bed velocities and the presence of a wave-induced streaming. Albeit the high quality of Klopman's (1994) experiments, they were mainly focused on the characteristics of the mean horizontal velocity. The tests with waves and currents provided no data on the Reynolds stresses.

More recently, Umeyama (2005) conducted experiments in a laboratory flume with a smooth bed for the purpose of measuring turbulence properties with only currents, only waves, and waves following and opposing currents, for different incident wave conditions (by varying the wave height and/or wave period). For the mean horizontal velocity, he presented the same conclusions as

* Corresponding author. Tel.: +351 218418128.
E-mail address: mjteles@gmail.com (M.J. Teles).

1463-5003/$ - see front matter © 2013 Elsevier Ltd. All rights reserved.
http://dx.doi.org/10.1016/j.ocemod.2013.04.006

Klopman (1994), but also identified the importance of the wave period. His results concerning near-bed mean velocities differ partially from Klopman's (1994) measurements.

In recent decades, many efforts have been made to improve the description of the combined effects of waves and currents. These studies are based on either purely analytical approaches with simple models of the wave boundary layer (in particular, relying on the concept of an eddy-viscosity), or numerical simulations to accommodate more sophisticated models of the primitive equations.

The work of Grant and Madsen (1979) follows the first approach, stating that the influence of waves on steady currents above the wave boundary layer can be parametrized by an apparent increase in the roughness experienced by the current. Additional examples of simplified wave boundary models include: Christoffersen and Jonsson (1985) with an eddy-viscosity approach (also a wealth of references on previous studies, particularly on purely oscillatory boundary layers), You (1996) with a parabolic distribution of the turbulence viscosity, Nielsen and You (1996), who explicitely take into account the wave induced Reynolds stresses, Huang and Mei (2003) who formulate a boundary-layer theory, and Yang et al. (2006) with a simplified mixing-length hypothesis.

Numerical approaches range from the inclusion of the Craik–Leibovich vortex force in the mean-current equations (Dingemans et al., 1996), to the Generalized Lagrangian Mean approach (GLM) (Groeneweg and Klopman, 1998; Groeneweg and Battjes, 2003), to a three-dimensional Navier–Stokes equation model (e.g. Olabarrieta et al., 2010).

The *Code_Saturne* model (Archambeau et al., 2004) is based on the three dimensional RANS (Reynolds Averaged Navier–Stokes) equations. The model was developed at the EDF R&D (Electricité de France, Research and Development) in Chatou, France and was initially designed for pressurized flows in large industrial installations. A number of adaptations had to be made to render the model suitable for the study of wave and current interactions considering turbulence effects in free surface flows. For these kinds of simulations, the Arbitrary Lagrangian Eulerian (ALE) methodology (Archambeau et al., 1999) was used.

Among the turbulence closure models available in the code, the choice was made to evaluate the first-order k–ϵ and k–ω models, which are widely used because of their simplicity, and the second-order Reynolds stress transport model R_{ij}—ϵ.

A tentative parameterisation of the turbulence viscosity in terms of the Ursell number will be proposed using the results of the numerical simulations obtained by *Code_Saturne*.

The paper is organised in the following way. After this introductory section, the laboratory measurements used to verify the model are introduced in Section 2. Section 3 describes the numerical model and the options chosen to configure the model. Section 4 analyses the accuracy of the mean horizontal velocity profiles, preceded by a sensitivity analysis of the turbulence closure models. In Section 5, a discussion of turbulence intensities modelling is presented. The conclusions are summarised in Section 6.

2. Laboratory data

Klopman (1994) carried out a series of laboratory experiments with two computer controlled wave boards (one generating waves and another absorbing the waves) and a flow circulation circuit able to provide a constant discharge of about $Q \approx 80$ l/s. The channel was 46 m long (x direction), 1 m wide (y direction) and the water depth was 0.5 m (z direction). Waves were generated with a second order signal to minimise free long waves. Based on the mean flow velocity, the flow was characterised by a Reynolds number of approximately 67,000.

Table 1
Wave heights and wave periods for the four test cases of Umeyama (2005).

Tests	*T1*	*T2*	*T3*	*T4*
Wave height (m)	0.0202	0.0251	0.0267	0.028
Wave period (s)	0.9	1	1.2	1.4

Numerical simulations were carried out for the test cases with currents only, waves only, and monochromatic waves following and opposing currents. The wave height was $H = 0.12$ m, and the wave period was $T = 1.44$ s. During each test, mean horizontal velocity profiles and horizontal velocity amplitudes were measured by a laser-Doppler velocimeter (LDV) at the middle of the channel ($x = 22.5$ m and $y = 0.5$ m). For the case with only currents, a description of the shear stress was also made through the LDV measurements.

The experiments from Umeyama (2005) were completed in a channel 25 m long and 0.7 m wide, with a water depth of 0.2 m. Regular waves were generated with a piston-type wave maker and dissipated with a wave absorber at the opposite end of the channel. Four combinations of wave height and wave period used in tests with only waves, waves following currents, and waves opposing currents (Table 1). The mean flow velocity in the channel was about 12 cm/s. For each test, the horizontal and vertical velocities were measured by a Laser Doppler Anemometer (LDA) 10.5 m from the wave generator. Mean velocity profiles and shear stresses were obtained.

For Klopman (1994) and Umeyama (2005), the relative wave heights were approximately $H/h \approx 0.24$ and $H/h \approx 0.1$, respectively, which qualifies them as intermediate non linear waves. With dimensionless depth $kh \approx 1$, these experiments are typically characterised as intermediate water depth.

3. *Code_Saturne* model

3.1. Introduction

Over the last few decades, increases in computing capacity and expansion of Computational Fluid Dynamics (CFD) software as a simulation tool has led to the possibility of solving complex and varied fluid flow problems, including the simulation of three-dimensional, time-varying flows.

The *Code_Saturne* (Archambeau et al., 2004) is a computational dynamic code that solves the Navier Stokes equations for laminar and turbulent flows in two and three dimensional domains. It is based on a Finite Volume approach that handles structured or unstructured meshes. The mass and momentum equations are written in a conservative form and then integrated over control volumes.

$$\frac{\partial \rho}{\partial t} + \nabla.(\rho u) = 0 \tag{1}$$

$$\frac{\partial \rho u}{\partial t} + \nabla.(\rho u \otimes u) = \nabla.\sigma + S_u \tag{2}$$

The additional momentum source term, S_u, can be prescribed by the user, ρ is the density, u the mean flow fluid velocity vector, and σ the stress tensor. For a turbulent flow, the stress tensor σ includes the effects of pressure, viscous stresses τ, and the turbulence Reynolds stress tensor R_{ij}. In order to close the system of Eqs. (1) and (2), the Reynolds stress tensor has to be modelled. In *Code_Saturne*, a large range of first and second order turbulence closure models have been implemented. While in a first-order turbulence model, the Reynolds stress tensor is linked to the mean flow velocity through the Boussinesq hypothesis and the turbulence viscosity approximation, in a second-order turbulence model, the Reynolds stresses are solved explicitly with transport type equations.

In the present work, the first-order two-equation models $k-\epsilon$ with linear production (Guimet and Laurence, 2002), and the $k-\omega$ SST (Menter, 1994), were evaluated in comparison to the second-order Reynolds stress transport model $R_{ij}-\epsilon$ SSG (Speziale et al., 1991).

The $k-\epsilon$ (Guimet and Laurence, 2002) and $R_{ij}-\epsilon$ SSG (Speziale et al., 1991) models are so-called *High Reynolds* number models. For these models, it is necessary to ensure that the thickness of the first computational cell near the wall is larger than the thickness of the viscous sublayer. Consequently, an analytical treatment (wall functions) is needed in the area near the wall. The $k-\omega$ SST (Shear Stress Transport) model proposed by Menter (1994) is a combination of a standard $k-\epsilon$ model that is suitable for the free flow and a standard $k-\omega$ model that exhibits better behaviour near the wall.

The first order turbulence models need additional equations to calculate the turbulence viscosity. The transport of the turbulence kinetic energy k (3) and turbulence dissipation rate ϵ (4) are examples of equations commonly used as closure, leading to the known $k-\epsilon$ turbulence model.

$$\rho\frac{\partial k}{\partial t}+\nabla.\left[\rho uk-\left(\mu+\frac{\mu_t}{\sigma_k}\right)\nabla k\right]=P+G-\rho\epsilon \tag{3}$$

$$\rho\frac{\partial \epsilon}{\partial t}+\nabla.\left[\rho u\epsilon-\left(\mu+\frac{\mu_t}{\sigma_\epsilon}\right)\nabla \epsilon\right] = C_{\epsilon1}\frac{\epsilon}{k}[P+(1-C_{\epsilon3})G]P-\rho C_{\epsilon2}\frac{\epsilon^2}{k} \tag{4}$$

$$v_t=\frac{\mu_t}{\rho}=C_\mu\frac{k^2}{\epsilon} \tag{5}$$

The fluid's dynamic molecular viscosity is expressed by μ, μ_t is the turbulence viscosity, P accounts for the production of the kinetic energy through mean shear stresses, G is the production-destruction tensor related to density effects, $\sigma_k=1$, $\sigma_\epsilon=1.3$, $C_{\epsilon1}=1.44$, $C_{\epsilon2}=1.92$ and $C_\mu=0.09$ are defined constants and finally $C_{\epsilon3}=0$ if $G\geqslant0$ and $C_{\epsilon3}=1$ if $G\leqslant0$.

In the $k-\omega$ SST model (Menter, 1994), Eq. (3) is solved for k, but the dissipation is estimated using a so-called specific dissipation $\omega=\frac{\epsilon}{\beta^* k}$, where $\beta^*=0.09$.

Contrary to first order turbulence models, in Reynolds Stress Models (RSM), the Reynolds stress transport Eq. (6) accounts for the directional effects of the Reynolds stress fields and does not include the eddy viscosity hypothesis. In Reynolds Stress Models (RSM) there are six transport equations for the six independent components of the Reynolds stress tensor and one equation for the dissipation rate.

$$\rho\frac{\partial R_{ij}}{\partial t}+\nabla.(\rho uR_{ij}-\mu\nabla R_{ij})=P_{ij}+G_{ij}+d_{ij}+\Phi_{ij}-\rho\epsilon_{ij} \tag{6}$$

$$\rho\frac{\partial \epsilon}{\partial t}+\nabla.(\rho u\epsilon-\mu\nabla\epsilon)=d_\epsilon+C_{\epsilon1}\frac{\epsilon}{k}[P+G_\epsilon]-\rho C_{\epsilon2}\frac{\epsilon^2}{k} \tag{7}$$

The turbulence production tensors related to mean shear stresses and gravity effects are P_{ij} and G_{ij}, respectively, Φ_{ij} is the pressure strain term, d_{ij} and d_ϵ are the turbulence diffusion terms, and ϵ_{ij} is the dissipation term (considered isotropic) (Archambeau et al., 2004). The ij subscripts refer to the tensor components with values 1, 2 and 3.

Free surface boundaries can be handled using a fixed-mesh or a moving-mesh approach. Muzaferija and Peric (1997) or Apsley and Hu (2003) show examples of applications of moving-mesh approach to modelling free-surface flows using the finite volume method. The *Code_Saturne* uses the Arbitrary Lagrangian Eulerian (ALE) methodology (Archambeau et al., 1999), which allows the mesh to follow the moving boundaries.

With this module, the Navier Stokes equations gain a new term which accounts for the vertical velocity of the mesh. At each time step, the mesh is updated with this velocity, constrained to guarantee a zero net mass flux at the free surface (10). The free surface vertical motion is distributed proportionally across the water column, approaching zero near the bottom. Fig. 1 shows an example of the free surface moving mesh when applying the ALE module.

3.2. Model setup

3.2.1. Wave generation and dissipation

To minimise undesirable free super-harmonic and sub-harmonic waves, a second-order piston-type wave boundary condition was applied at one end of the channel. Thus, an horizontal movement of the mesh was imposed at the lateral wall in order to produce waves. Waves propagated in positive x-direction. The following expression for the wave board motion displacement $X_0(t)$ in Eq. (8) (Dean and Dalrymple, 1991) was introduced:

$$X_0(t)=\frac{H}{2m_1}sin\left(\frac{2\pi}{T}t\right)+\frac{H^2}{32h}\left(\frac{3cosh(Kh)}{sinh^3(Kh)}-\frac{2}{m_1}\right)sin\left(2t\frac{2\pi}{T}\right) \tag{8}$$

with m_1 given by:

$$m_1=\frac{4sinh(Kh)}{sinh(2Kh)+2Kh}\left[sin(Kh)+\frac{(1-cosh(Kh))}{Kh}\right] \tag{9}$$

K represents the wave number, h the water depth, H the wave height, T the wave period, and t the time. To avoid a sudden movement of the mesh and thus mesh crossover, the signal at the lateral boundary (8) was progressively imposed in time.

The energy of waves can be dissipated if the waves propagate into a more viscous fluid. Following this idea, the numerical channel was extended by about six wave lengths with a less refined mesh and a linear increasing viscosity distribution was imposed in the extension.

3.2.2. Mesh generation

The mesh generation is subject to a number of conditions that the modeller has to take into account. On one hand, in order to ensure a good representation of the waves, it is necessary to have about 10 cells per wavelength. On the other hand, the mesh resolution can not be too fine next to the moving wall to avoid mesh crossover and the divergence of the simulation.

Mesh resolution in the vicinity of boundaries where a no-slip condition applies (i.e. near the bottom in our computations) requires special attention when using CFD codes. There are basically two main approaches that can be followed by such codes: in the first one, usually referred to as *Low Reynolds* number model, the

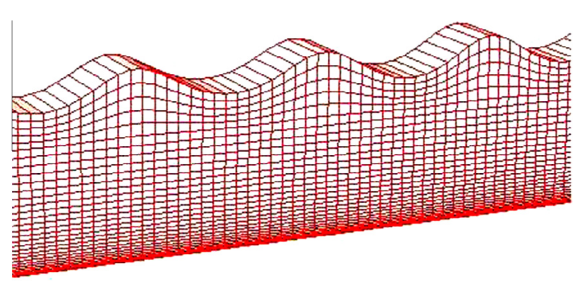

Fig. 1. Model grid. Application of the ALE module to the free surface moving mesh representation.

CFD model is used throughout the boundary layers (including the viscous sublayer in the vicinity of the boundary) and above, with a very refined grid in order to resolve the structure of the flow (which is strongly sheared) when approaching the boundary. In the second one, the actual use of the CFD code (where the first grid point lies) starts at a given (small) distance from the wall and an additional wall function is applied in order to correctly handle the viscous effects at the boundary. In this case, the resolution of the grid close to the boundary is coarser compared to the previous approach. This approach is usually referred to as *High Reynolds* number model, or "wall function approach". With the present version of *Code_Saturne*, we decided to adopt the second modelling strategy (*High Reynolds* number model) and to use a wall function close to the bottom. This was motivated by two main reasons: first, *Code_Saturne* is designed to be used preferably with this modelling strategy and more experience is available on this side, and secondly we wanted to keep the computational effort moderate for the first step of our research project.

Since *High Reynolds* number models were used, there are some constraints on the relative size of the cells near the bottom. It is necessary to ensure that $z^+ > 2.5$, but it is preferential that $30 < z^+ < 100$, where z^+ is the dimensionless z-coordinate normalised by the thickness of the viscous sublayer $\left(\delta = \frac{\nu}{u_*}\right)$. At the same time, some important effects were analysed in this region, such as the influence of the roughness on the vertical profile of the measured quantities, so adequate spatial resolution was required. To satisfy these conditions, the vertical discretization of the mesh had a varying resolution of 0.005 m $< \Delta z <$ 0.025 m for the simulations of Klopman's channel and 0.001 m $< \Delta z <$ 0.005 m for the simulations of Umeyama's channel.

In the end, the computational domains for Klopman's and Umeyama's channels had approximately 18,500 and 24,000 cells, respectively.

3.2.3. Boundary conditions at the free surface and bottom

Recently, Cozzi (2010) adapted the ALE method for representing wave propagation in free surface flows. One of the conditions imposed at the free surface, to ensure zero net mass flux, is represented by the following expression:

$$w = \frac{u.S}{e_z.S} = \frac{\dot{m}_{fs}}{\rho S_z} \tag{10}$$

The vertical velocity of the mesh is represented by w, $\dot{m}_{fs}$ is the mass flux when the free surface is represented with a fixed mesh, and S_z is the vertical component of the unit free surface, S.

The modifications made by Cozzi (2010) were appropriate for a perfect fluid and potential flow, which is typical of a waves only test case. In the present study, the *Code_Saturne* was applied with the objective to study wave–current interactions taking into account the effects of turbulence on free surface flows. For this purpose, an additional condition (11), proposed by Celik and Rodi (1984), had to be imposed on the free surface:

$$\epsilon = \frac{k^{3/2}}{h\alpha} \tag{11}$$

The turbulence dissipation, ϵ, and the turbulence kinetic energy, k, are the values at the free surface and $\alpha = 0.18$ is an empirical constant. Although the RSM model does not compute explicitly the turbulence energy k, this variable is estimated as half the sum of the normal stresses (see point 5.2, (17)). In the $k-\omega$ model, ϵ is replaced by $\omega\beta^* k$ in (11).

This boundary condition accounts for the reduction of the length scale of turbulence near the free surface, which is physically consistent and has been observed experimentally by Nezu and Rodi (1986). With this boundary condition, the turbulence dissipation, which determines the turbulence length scale, will be higher than the value obtained when using a zero-gradient surface boundary condition (Nezu and Nakagawa, 1993). Hence from Eq. (5), it can be seen that the eddy viscosity decreases toward the free surface.

Additionally, a Neumann condition for the Reynolds stress is defined at the free surface:

$$\frac{\partial R_{ij}}{\partial z} = 0 \tag{12}$$

Analogous to the above equation, a zero flux condition is also used for the turbulence kinetic energy. At the bottom boundary, a rough wall function (13) defining the relation between the tangential velocity of the fluid relative to the wall $(u_{\tau,I})$ and the friction velocity at the wall (u_*) was imposed (incorporated already in *Code_Saturne*):

$$\frac{u_{\tau,I}}{u_*} = f(z_p) = \frac{1}{\kappa} ln\left(\frac{z_p + z_0}{z_0}\right) \tag{13}$$

The von Karman constant is $\kappa = 0.41$, z_p is a distance from the wall defined by the size of the first cell and z_0 is a parameter related to the wall roughness that has to be defined by the user.

The following boundary conditions are applied near the wall for the other turbulence variables:

$$\nabla(R_{ii}).n = 0; \quad R_{12} = u_* u_k; \quad R_{13} = R_{23} = 0 \tag{14}$$

$$\epsilon = \frac{u_k^3}{\kappa z} \tag{15}$$

$$k = \frac{u_k^2}{\sqrt{C_\mu}} \tag{16}$$

The unit vector normal to the boundary, oriented outwards, is represented by n and u_k is an estimate of u_* obtained from the turbulence kinetic energy.

4. Mean horizontal velocity profile

4.1. Turbulence closure model sensitivity

4.1.1. The "only currents" case

An important step evaluation of the ability of a full RANS equations model (e.g. *Code_Saturne*) to represent wave–current interactions, is a sensitivity study of the built-in turbulence closure models. Throughout this sub-section, the Klopman (1994) data was used for that purpose. Klopman (1994) found in the only current experiment a value of $z_0 = 0.04$ mm. Therefore, the same value was imposed in *Code_Saturne*.

The numerical model output corresponds to the phase-averaged values, from which it was possible to estimate the contributions of the mean flow and the waves. For the cases with waves propagating in the channel, results were analysed for fifty wave cycles within the 600 s of the total simulation time.

It should be highlighted that this sensitivity test is made with the default parameters set in the *Code_Saturne* turbulence models. Thus, no optimisation of the constants of the model was attempted for any of the turbulence closure models. For all models, the same mesh was used, and the same free surface (11) and bottom (13) boundary conditions were imposed. The time step for each simulation was set to 0.02 s.

The first test case had only currents. The simulation runs until a stationary current is achieved. Fig. 2 shows the comparison of the mean horizontal current profiles calculated with the $k-\epsilon$, $k-\omega$ and $R_{ij}-\epsilon$ turbulence closure models. Good agreement is found between the simulations with *Code_Saturne* and the laboratory data.

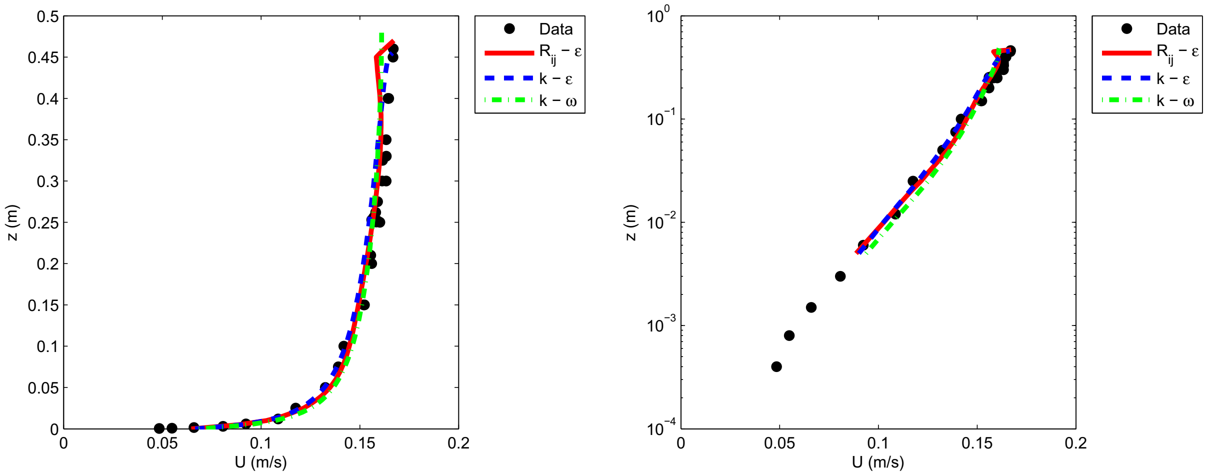

Fig. 2. Vertical profiles of the mean horizontal velocity for only currents: linear scale (left) and semi-log scale (right). Data from Klopman (1994).

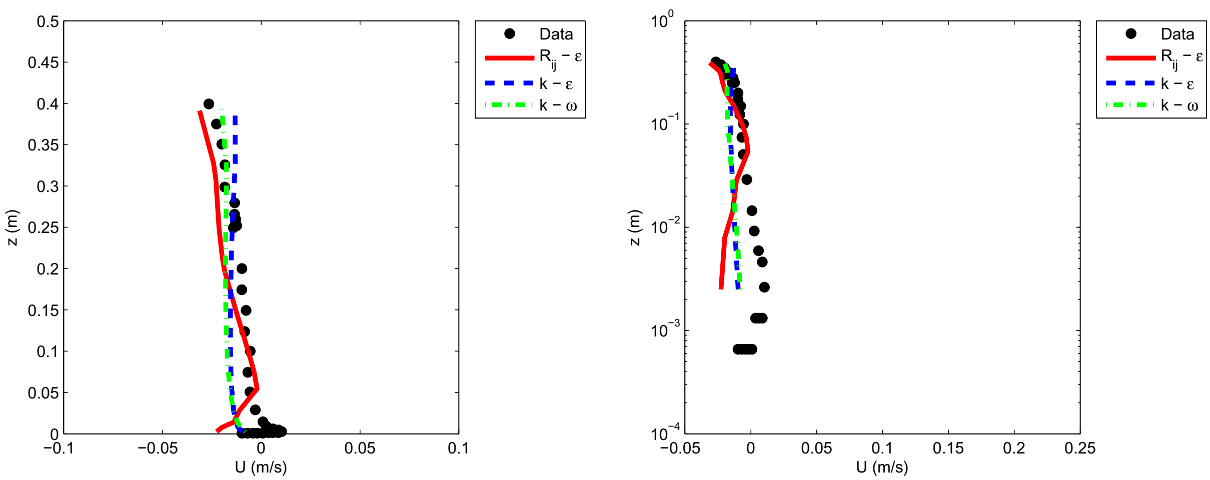

Fig. 3. Vertical profiles of mean horizontal velocity for waves only: linear scale (left) and semi-log scale (right). Data from Klopman (1994).

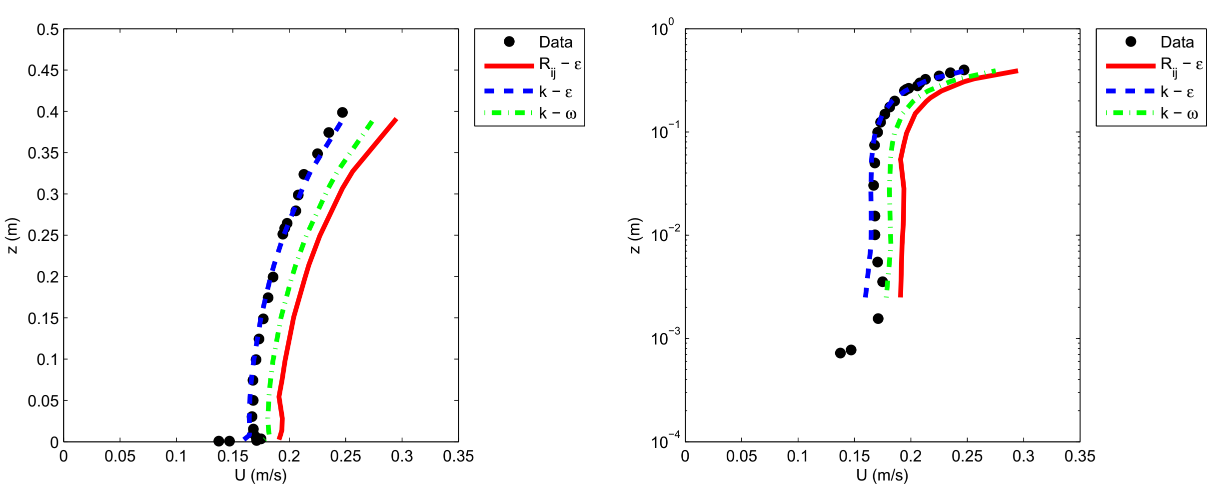

Fig. 4. Horizontal velocity amplitude profile for only waves: linear scale (left) and semi-log scale (right). Data from Klopman (1994).

Near the free surface, there is a slight curvature in the vertical profile of the mean horizontal velocity when the R_{ij}–ϵ model is applied. This behaviour is not observed with the two other turbulence models. It could be due to the impact of the side walls on the mean flow and the three-dimensionality of the flow, since the ratio between the channel width (B) and water depth

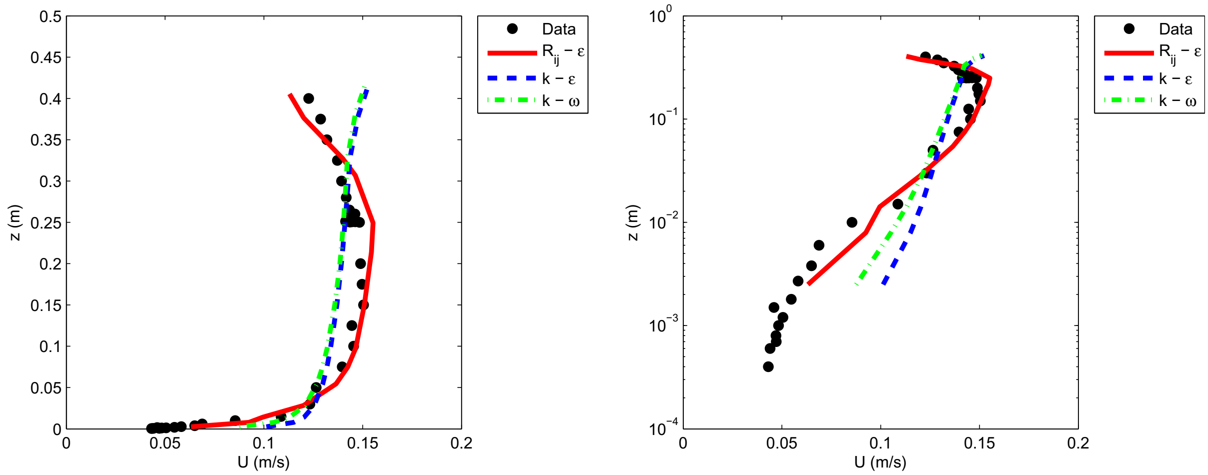

Fig. 5. Vertical profiles of mean horizontal velocity for waves following currents: linear scale (left) and semi-log scale (right). Data from Klopman (1994).

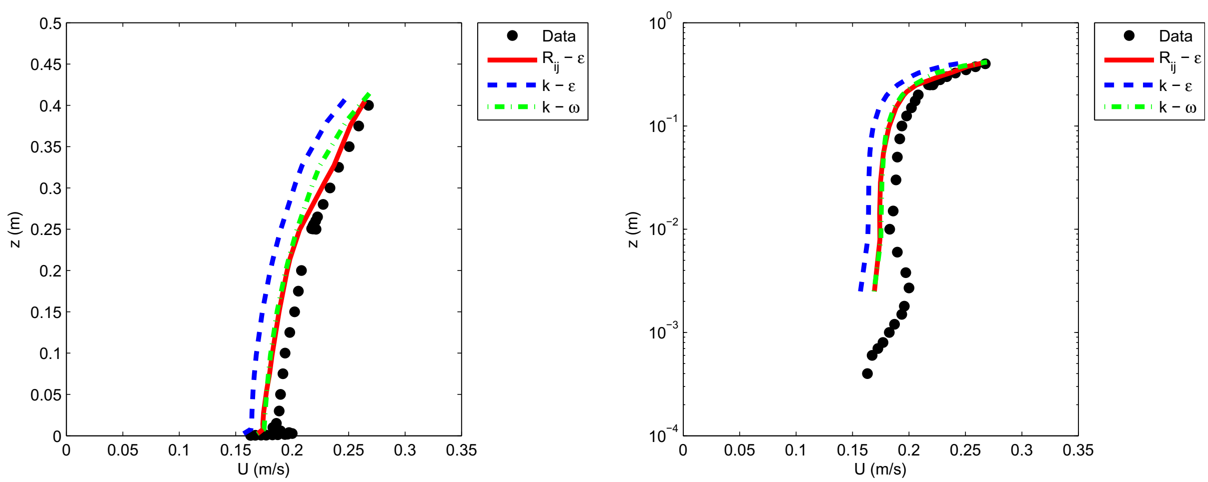

Fig. 6. Horizontal velocity amplitude profile for waves following currents: linear scale (left) and semi-log scale (right). Data from Klopman (1994).

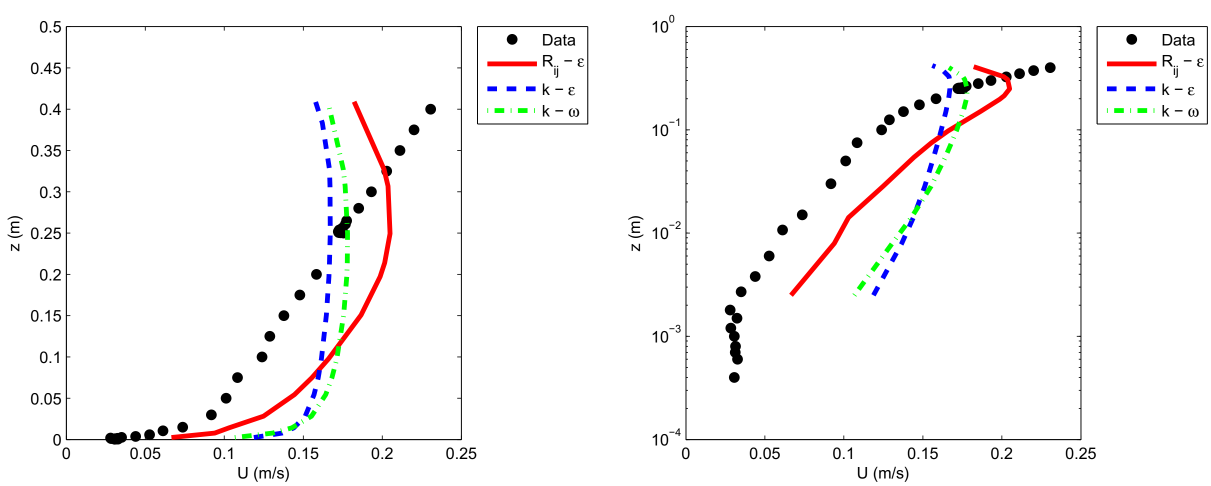

Fig. 7. Vertical profiles of mean horizontal velocity for waves opposing currents: linear scale (left) and semi-log scale (right). Data from Klopman (1994).

(h) is $\frac{B}{h} = 2$. This effect was also observed by Song (1994) for a turbulent current without waves and with the same range of values for $\frac{B}{h}$.

Of the three turbulence closure models, it is possible that the R_{ij}–ϵ model is the only one capable of reproducing these effects, since it takes into account the turbulence anisotropy.

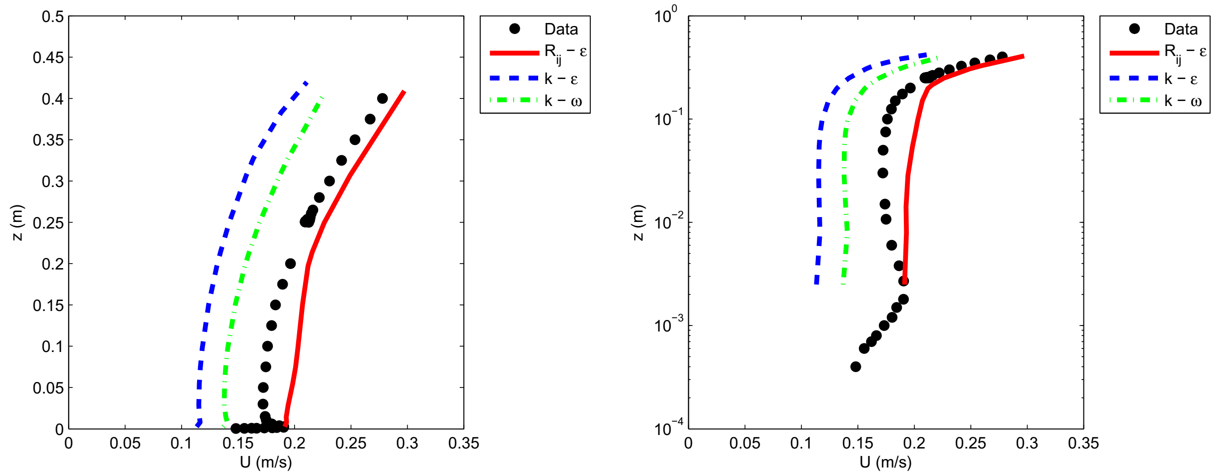

Fig. 8. Horizontal velocity amplitude profile for waves opposing currents: linear scale (left) and semi-log scale (right). Data from Klopman (1994).

4.1.2. The "only waves" case

The second test case investigated the propagation of waves (along the positive x axis) in the channel without currents. Fig. 3 presents the numerical results and the experimental data for the mean horizontal velocity profiles. Near the bed, around $z \approx 0.02$ m, the mean horizontal velocity changes sign, becoming negative. Below this level, there is a layer where the velocity is positive and in the direction of wave propagation, representing wave-induced streaming. These are second-order steady mean velocity fields that arise in any oscillatory flow. They are a consequence of viscosity and spatial variation of the velocity field outside this layer. This was first described by Longuet-Higgins (1953) for sinusoidal surface water waves. Holmedal et al. (2009) studied different mechanisms causing streaming, in particular, the importance of the mass transport beneath second-order Stokes waves.

On Fig. 3 it can be observed that neither model can reproduce the wave streaming effect. Nevertheless the second order R_{ij}—ϵ model seems to fit better the observations. The negative velocities in the middle of the water column are due to the undertow, and they compensate for the positive mass flux between the wave trough and the wave crest (i.e. the Stokes drift (not shown here)) since conservation of mass is guaranteed.

The horizontal velocity amplitude profile is presented in Fig. 4. The k—ω and R_{ij}—ϵ models overestimate the horizontal velocity amplitude. Even though, the key features of the vertical profile, i.e. the cosine hyperbolic shape above the boundary layer and the overshooting before reaching this shape, are fairly well reproduced.

4.1.3. The "waves following currents" case

The vertical profile of the mean horizontal velocity is significantly changed by the presence of the waves, as seen by comparing Fig. 5 with Fig. 2.

In the case of waves following currents, the velocity shear in the upper half of the water column decreases and become negative. Fig. 5 shows that the R_{ij}—ϵ turbulence model was the only model capable of simulating the reduction in the velocity near the free surface. The simulations agreed well with the experiments not only near the bottom but also near the free surface.

The change in the velocity gradient near the free surface can be caused by different effects. A number of authors (e.g. Groeneweg and Klopman, 1998; Groeneweg and Battjes, 2003; Huang and Mei, 2003; You, 1996; Nielsen and You, 1996) attributed this change in the mean horizontal velocity profile mainly to the wave

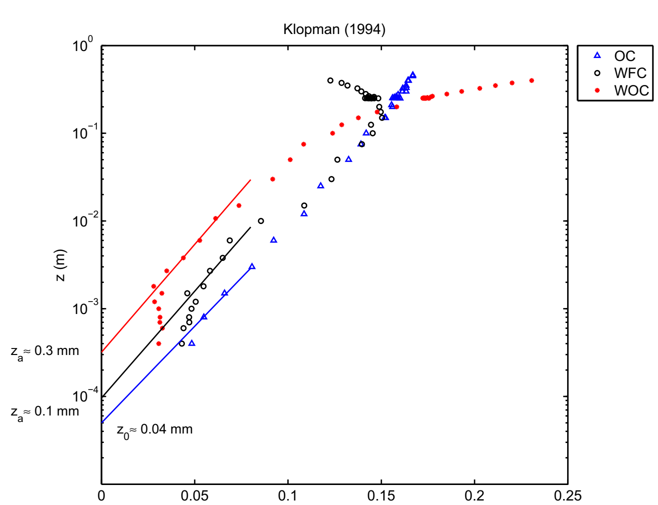

Fig. 9. Comparison of the vertical profiles of the mean horizontal velocity in a semi-log scale for the cases "only current " (OC), "waves following the current " (WFC) and "waves opposing the current " (WOC). Data from Klopman (1994).

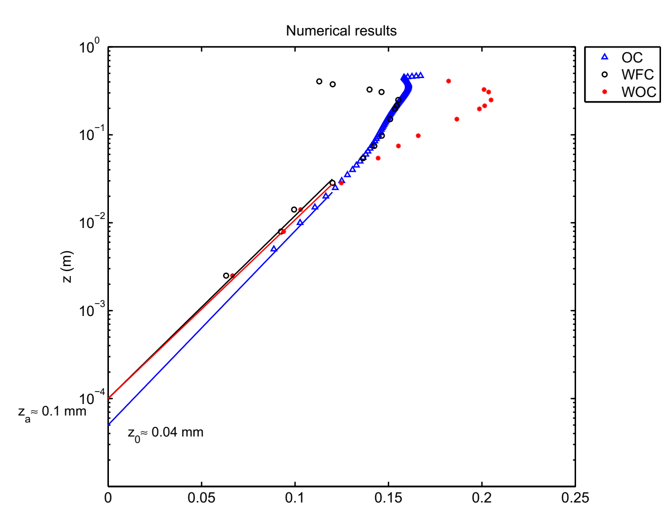

Fig. 10. Numerical results of the vertical profiles of the mean horizontal velocity in a semi-log scale for the cases "only current " (OC), "waves following the current " (WFC) and "waves opposing the current " (WOC).

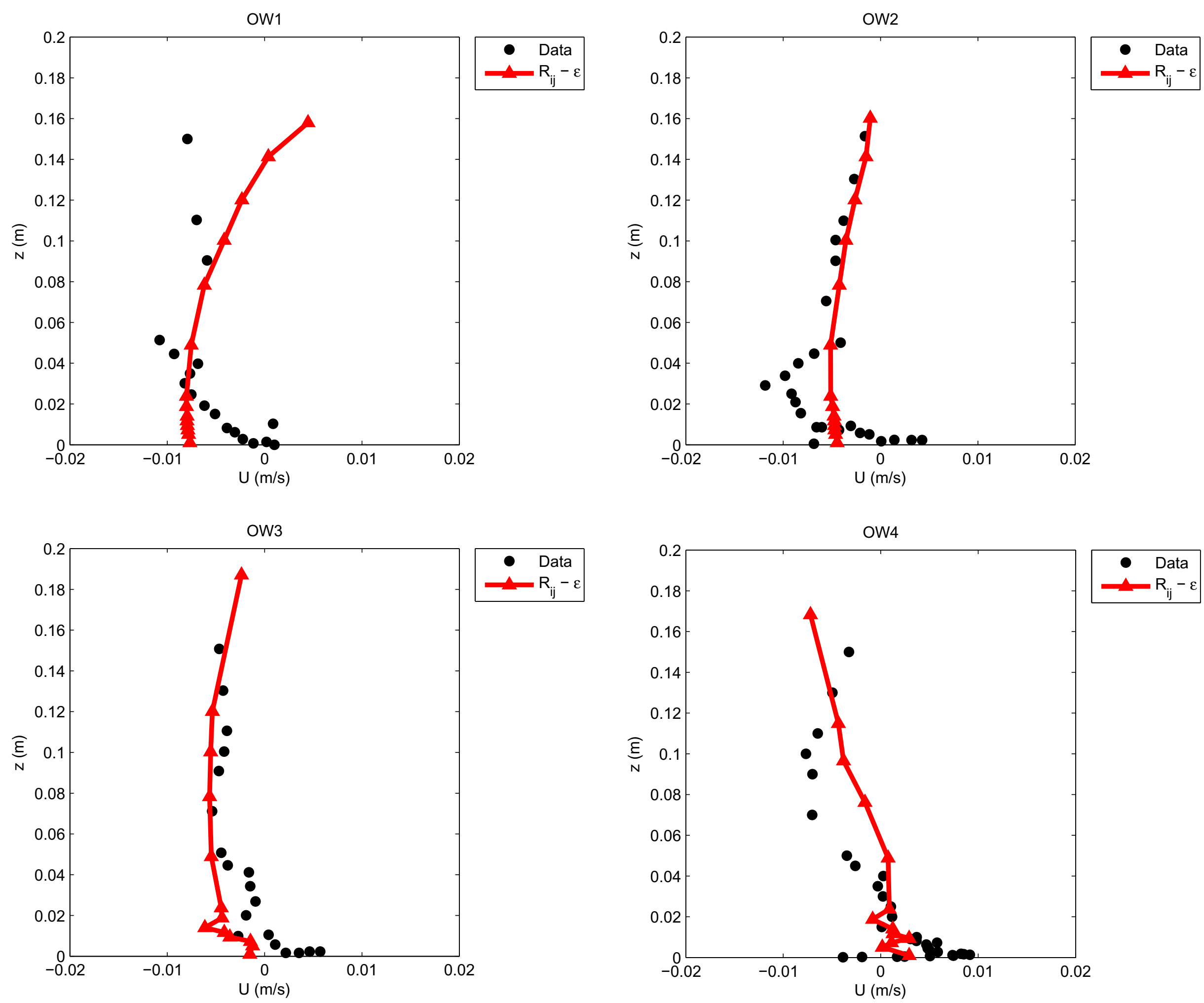

Fig. 11. Mean velocity vertical profile for only waves: OW1 (H = 0.0202 m; T = 0.9 s); OW2 (H = 0.0251 m; T = 1 s); OW3 (H = 0.0267 m; T = 1.2 s) and OW4 (H = 0.0280 m; T = 1.4 s). Data from Umeyama (2005).

induced Reynolds stress when waves propagate in a flume. Due to oscillations induced by the superposition of waves the mean flow is modified.

When waves are superposed on a turbulent current flowing in the same direction, the current shear velocity is positive. When approaching the free surface (where the wave induced stresses are more important) the wave related propagation contributions have opposite sign with the current contribution resulting in a decrease of the mean velocity shear. It can be even negative as in the present study.

Yang et al. (2006) analysed other possible effects, such as the non-uniformity of the flow (existence of a free surface slope along the channel) and/or secondary currents induced by sidewall effects. They concluded that both contributions also caused a change in mean horizontal velocity profile.

The decay of waves when propagating along the channel could cause a variation of the mean surface elevation and thus giving a non-uniformity character to the flow.

Klopman (1997) repeated the same experiments as in Klopman (1994), but this time he completed measurements along the cross section. He concluded that the secondary circulation cells predicted by the Craik–Leibovich vortex force theory existed in the flume. However, Groeneweg and Battjes (2003) concluded that this effect have a secondary influence on the change of the mean horizontal velocity profile.

The first order turbulence models, k–ϵ and k–ω, were not able to reproduce the reduction of mean horizontal velocity near the free surface. The accurate results obtained by the R_{ij}–ϵ model are a natural consequence of the fact that the turbulence dissipation and the Reynolds stresses are computed explicitly and hence the model is able to take into account the anisotropy of the flow. In the first-order turbulence closure models, the Boussinesq approximation does not take into account the anisotropy of the flow due to the isotropic eddy viscosity assumption.

Comparing the right panels of Figs. 2 and 5 (semi-logarithmic scale) a reduction of the near-bed velocities is observed. Again, the R_{ij}–ϵ model simulations approach the data better.

Fig. 6 shows the horizontal velocity amplitude profile. All of the numerical simulations slightly underestimate the measurements, and the R_{ij}–ϵ approach shows the best performance. The above-mentioned overshooting is not well represented in this case.

4.1.4. The "waves opposing currents" case

In the case of waves opposing the current, an increase in the velocity near the surface was observed by Klopman (1994) and others, such as Kemp and Simons (1983). Similar to the case of waves following currents, the R_{ij}–ϵ model showed the best performance, even if the increase of the mean velocity in the upper part of the water column was slightly underestimated and the mean current profile in the middle of the water column was overesti-

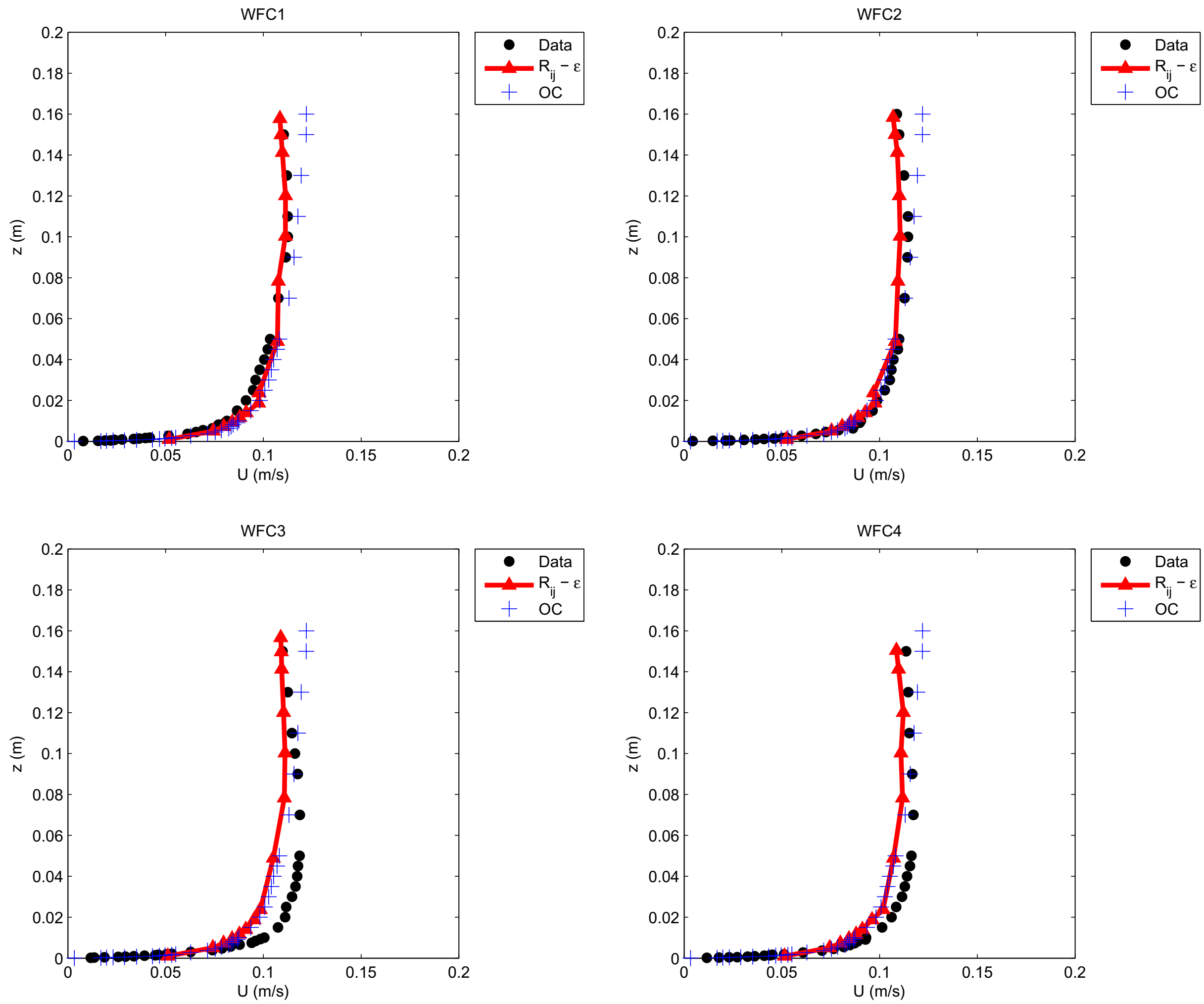

Fig. 12. Mean velocity vertical profile for only currents (OC) and for waves following currents: WFC1 ($H = 0.0202$ m; $T = 0.9$ s); WFC2 ($H = 0.0251$ m; $T = 1$ s); WFC3 ($H = 0.0267$ m; $T = 1.2$ s) and WFC4 ($H = 0.0280$ m; $T = 1.4$ s). Data from Umeyama (2005).

mated (Fig. 7). Nevertheless, the mean horizontal velocity profile showed good agreement through the water column.

Contrary to the waves following the current case, when waves are opposing the mean flow, the current shear velocity is negative and therefore with the same sign of wave induced Reynolds stress contribution. Hence, the mean velocity gradient is going to increase when approaching the free surface.

The mean horizontal velocity amplitude profile in the case of waves opposing the current is shown on Fig. 8. It can be verified that the $k-\epsilon$ and $k-\omega$ models underestimate it comparing to the measurements. Even if slightly overestimated, the $R_{ij}-\epsilon$ shows the best results.

4.2. Brief discussion about the apparent roughness

For combined waves and currents, the variable z_a is the analogue of the standard roughness length z_0. It is an apparent roughness that plays an important role in the interaction of waves and currents with the bottom boundary layer. It was already identified by Lundgren (1972) by the association of a reduction of the current velocity in the presence of waves, to the increase of the viscosity in the wave boundary layer. It was formalised by Grant and Madsen (1979) and has been used since by a number of researchers (Christoffersen and Jonsson, 1985; Soulsby et al., 1993; Fredsøe et al., 1999; Houwman and van Rijn, 1999; Perlin and Kit, 2002; Holmedal et al., 2003; Huang and Mei, 2003; Van Rijn, 2007; Olabarrieta et al., 2010). In these studies, it is clear that the apparent roughness is the dominant roughness factor and a measure of the effect of the waves on the mean current profile above the boundary layer.

The wave induced velocity field increases the turbulence in the wave boundary layer and a reduction of near-bed mean horizontal velocities is observed. This effect is equivalent to an increase of the roughness of the physical bottom boundary and could be parametrized with a high value of the Nikuradse roughness or, which is equivalent, an additional roughness experienced by the current (see Fredsøe et al., 1999 for an account of the mechanism responsible for the change of the apparent roughness).

The experimental data obtained by Klopman (1994) showed an increase in the apparent roughness when waves opposed the current as compared to the case with only currents. No such clear increase could be identified in the case of waves following the current. In Fig. 9 the values of z_a shown were obtained by linear extrapolation of the mean horizontal velocities estimated from the data.

As pointed out, in the present study *Code_Saturne* was applied using a *High Reynolds* number modelling strategy (i.e. a wall function approach in the vicinity of the bottom) and therefore the model is not able to fully resolve the bottom boundary layer. It can be seen from Fig. 10 that the values obtained by linear extrapolation of the mean horizontal velocities estimated from the *Code_Saturne*

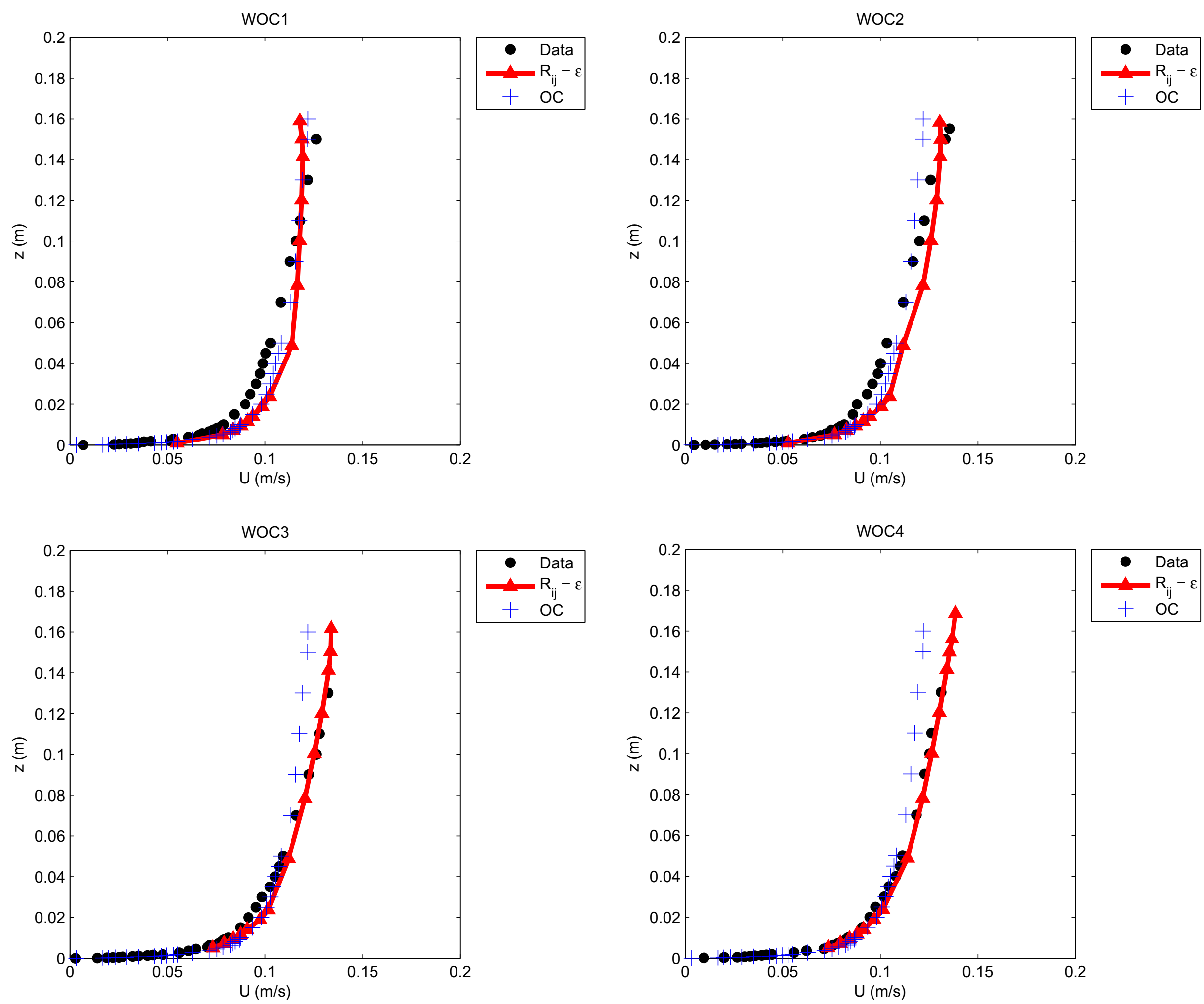

Fig. 13. Mean velocity vertical profile for only currents (OC) and for waves opposing currents: WOC1 (H = 0.0202 m; T = 0.9 s); WOC2 (H = 0.0251 m; T = 1 s); WOC3 (H = 0.0267 m; T = 1.2 s) and WOC4 (H = 0.0280 m; T = 1.4 s). Data from Umeyama (2005).

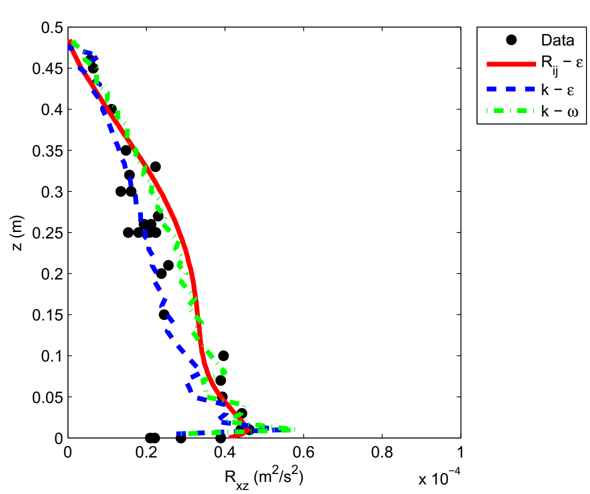

Fig. 14. Vertical profiles of the Reynolds shear stress $R_{xz} = -\langle u'w' \rangle$ for the "only currents" case using the three turbulence closure models in *Code_Saturne*. Data from Klopman (1994).

model are higher than the initially imposed physical roughness (z_0), both for the waves following and waves opposing the currents cases. This increase is related to the apparent roughness concept.

4.3. Influence of external parameters

4.3.1. The "only waves" case

A sensitivity test similar to the one presented previously (Sections 4.2.2–4.2.4) concerning the choice of the turbulence closure model was also made for Umeyama's experiments. The same conclusions were achieved and so they are not presented here. More details can be found on Teles et al. (2013). Therefore, the $R_{ij}-\epsilon$ turbulence closure model will be used in the *Code_Saturne* for the remainder of this section.

In an experimental flume (described in Section 2) with waves and currents, Umeyama (2005) measured the vertical profile of the mean horizontal velocity and Reynolds stresses. Four different wave heights and wave periods were considered for the test cases with only waves, waves following currents, and waves opposing currents. The channel had a smooth bed and, contrary to Klopman's experiments, the z_a parameter did not have an important role.

Fig. 11 shows the vertical distribution of the mean horizontal velocity for four different wave conditions (in the case of only waves). Again, the model is capable of predicting well the mean horizontal velocity profiles for each case. It is also evident that when the wave height increases, the wave boundary layer effects become more significant.

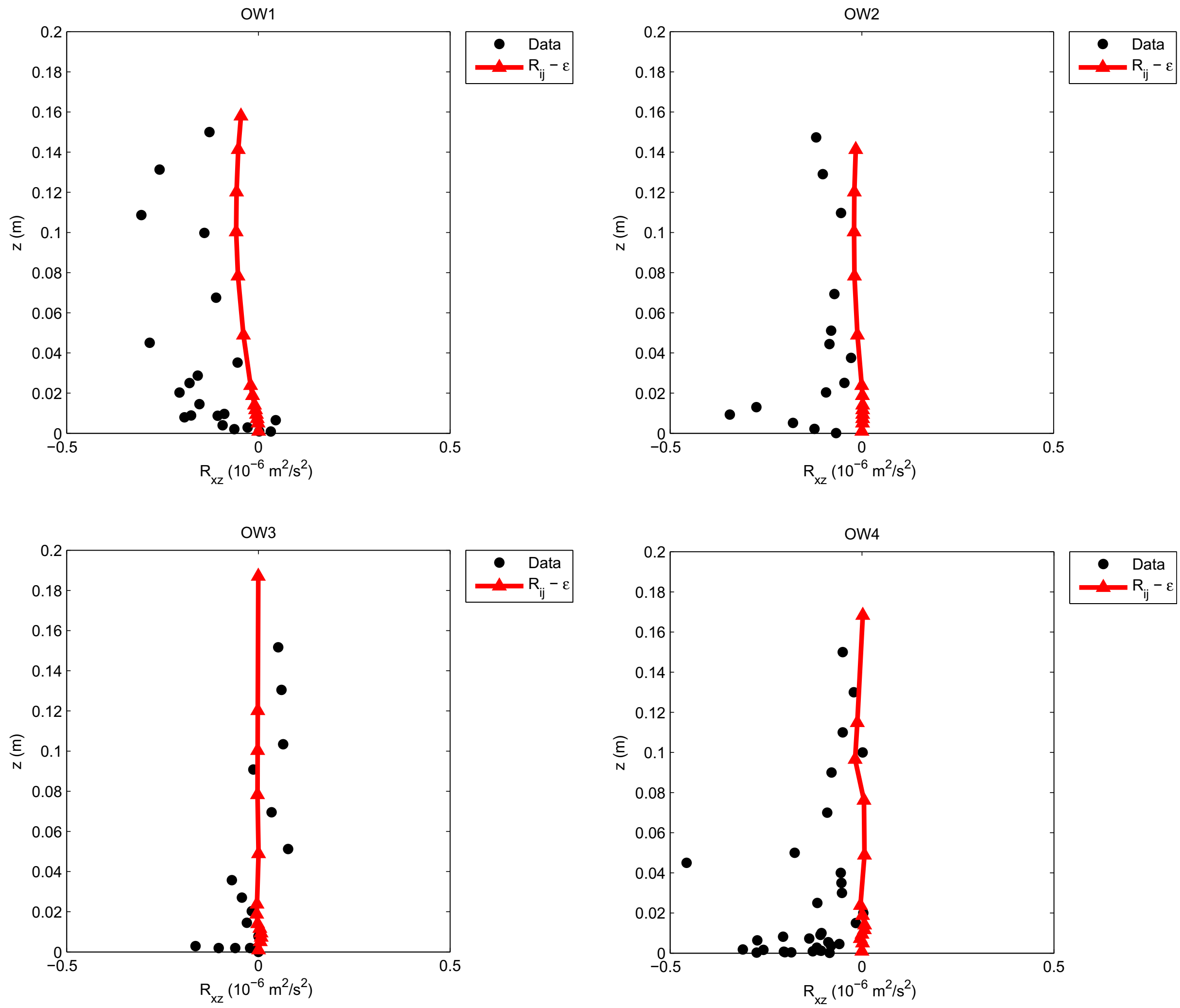

Fig. 15. Vertical profiles of the Reynolds shear stress $R_{xz} = -\langle u'w' \rangle$ for "only waves" cases: OW1 (H = 0.0202 m; T = 0.9 s); OW2 (H = 0.0251 m; T = 1 s); OW3 (H = 0.0267 m; T = 1.2 s) and OW4 (H = 0.0280 m; T = 1.4 s). Data from Umeyama (2005).

4.3.2. The "waves following currents" case

Fig. 12 shows the mean horizontal velocity vertical profile when waves are superposed on a turbulent current. For the four different conditions of waves following currents, the velocity increases near the bed and then decreases near the free surface.

The phase-averaged Reynolds stresses induced by the waves represent the phase-averaged correlation between the horizontal and vertical velocities. In intermediate waters (like in these experiments), Olabarrieta et al. (2010) pointed out that as the wave height increases, this correlation increases, and a sharp decrease in the mean horizontal velocity can be seen. However, as the wave period increases, the vertical component of the particle motion decreases, causing a reduction of Reynolds stresses. The effects of the wave height and wave period oppose each other, which could explain why the decrease in mean velocity does not vary significantly between the experiments. When compared with the experimental results, it can be concluded that the *Code_Saturne* model reproduces well these effects.

4.3.3. The "waves opposing currents" case

For waves opposing currents (Fig. 13), the velocity profile is initially logarithmic, but it begins to deviate, and the velocity shear increases near the free surface. The mean velocity gradient seems to increase with an increase in wave height and wave period. This behaviour is very well reproduced by the numerical simulations in the two more energetic cases. However for the two lower wave conditions some discrepancies are found. Near the free surface the modelled velocity gradient becomes even negative ($H = 0.0202$ m) or approaches to zero ($H = 0.0251$ m). Just above the boundary layer the slight decrease in $\frac{dU}{dz}$ cannot be observed in the model results.

5. Vertical profiles of Reynolds stresses and turbulence viscosity

5.1. Vertical profile of the R_{xz} Reynolds stress

5.1.1. The "only currents" case

It was also of great interest to analyse the capacity of the *Code_Saturne* model to reproduce the vertical profile of the Reynolds shear stress $R_{xz} = -\langle u'w' \rangle$, and therefore to understand better the different mechanisms that occur in a turbulent flow, such as in a wave–current environment. Firstly, the vertical profile of the Reynolds stress R_{xz} with "only currents" was tested. A comparison was made between the shear stress profile obtained by Klopman (1994) and the results of the *Code_Saturne* model using the three turbulence closure models evaluated in Section 4.21. Fig. 14 shows that the results obtained with both the k–ϵ, k–ω and R_{ij}–ϵ models agree well with Klopman's data for the entire water column.

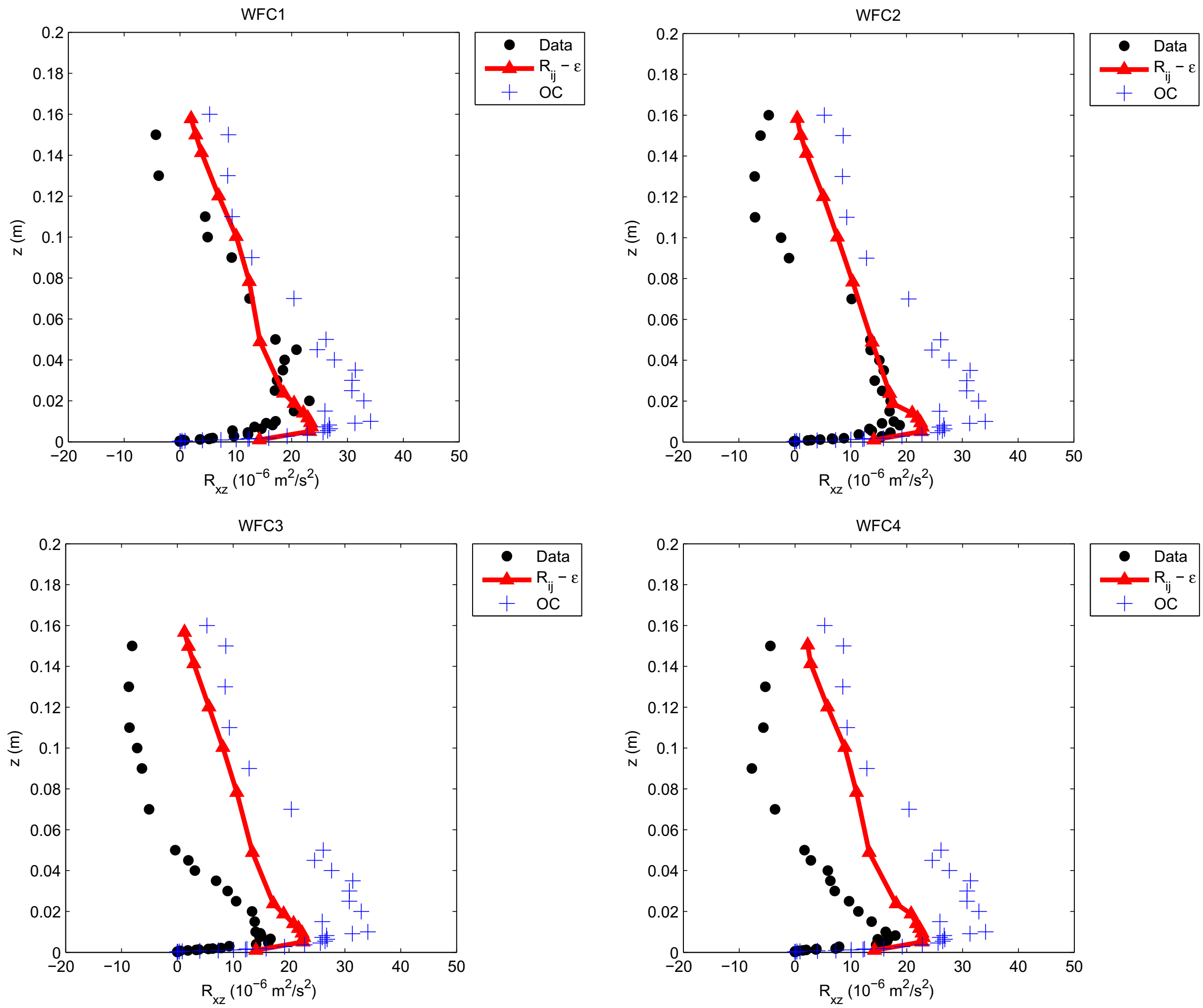

Fig. 16. Vertical profiles of the Reynolds shear stress $R_{xz} = -\langle u'w' \rangle$ for only currents (OC) and for "waves following currents" cases: WFC1 (H = 0.0202 m; T = 0.9 s); WFC2 (H = 0.0251 m; T = 1 s); WFC3 (H = 0.0267 m; T = 1.2 s) and WFC4 (H = 0.0280 m; T = 1.4 s). Data from Umeyama (2005).

5.1.2. The "only waves" case

Since the Klopman (1994) shear stress data only include the currents only case, the remainder of the comparisons in this section will be completed with the Umeyama (2005) data. The numerical simulations of the *Code_Saturne* will use the R_{ij}—ϵ closure approach. As seen in Fig. 15, the shear stress is almost zero when there are only waves in the flume. In fact, in the only waves case, the flow is characterised by an almost potential flow. It can be verified that the model is able to reproduce the expected monotonic behaviour over the water column. Also the close to zero values computed are what to be expected. However, it can be concluded that in the bottom boundary layer *Code_Saturne* may have some difficulties in representing the shear stress when only waves are present.

5.1.3. The "waves following currents" and "waves opposing currents" cases

Figs. 16 and 17 present the changes of the vertical profile of the Reynolds stress R_{xz} when progressive waves are superposed on a current in a flume. The striking feature in Figs. 16 and 17 is the decrease in the Reynolds shear stress in comparison with the values obtained from the only currents experiment (indicated by the + symbol in these figures). The superposition of waves caused a reduction in the turbulence stresses, not only near the bottom, but also over the whole water column. This behaviour was also observed by Kemp and Simons (1982). They refer that somehow the generation of turbulence is also periodic (because of the waves). For this reason part of the turbulence intensities are going to be absorbed into the phase averaged values and do not appear as measured turbulence intensities.

The Reynolds stress intensity has the same average order of magnitude over the water column and does not change significantly with the wave direction. The numerical simulations reproduce well this behaviour, especially in the "waves opposing currents" case (Fig. 17).

In Fig. 16, a difference in the modelled and measured Reynolds stresses is observed in the more energetic cases. In particular, the model does not simulate the observed reverse in sign of the Reynolds stress near the surface.

In general, the *Code_Saturne* had some difficulties modelling the shear stress near the free surface. The observed differences could be caused by neglecting to model the shear stress at the free surface due to interactions between the water and the air (Dore, 1978). In and above the wave boundary layer (in the lower panels of Fig. 16) no reasons were found for the mismatches observed between the numerical results and experimental data.

5.2. Vertical profile of eddy (turbulence) viscosity

As previously mentioned, analytical expressions for the vertical profile of the turbulence viscosity in environments with waves and

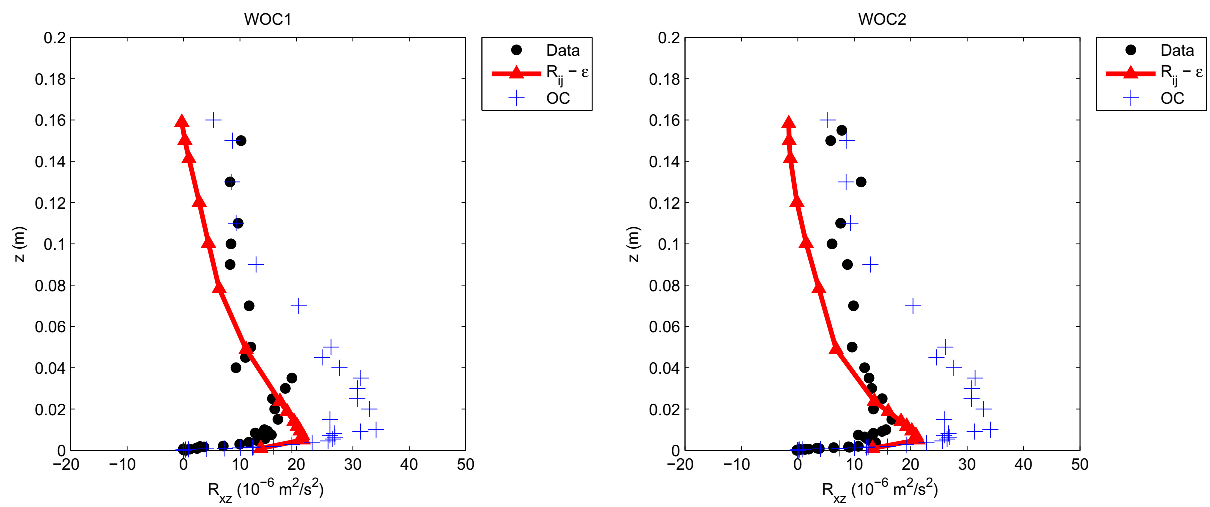

Fig. 17. Vertical profiles of the Reynolds shear stress $R_{xz} = -\langle u'w' \rangle$ for only currents (OC) and for "waves opposing currents" cases: WOC1 (H = 0.0202 m; T = 0.9 s); WOC2 (H = 0.0251 m; T = 1 s); WOC3 (H = 0.0267 m; T = 1.2 s) and WOC4 (H = 0.0280 m; T = 1.4 s). Data from Umeyama (2005).

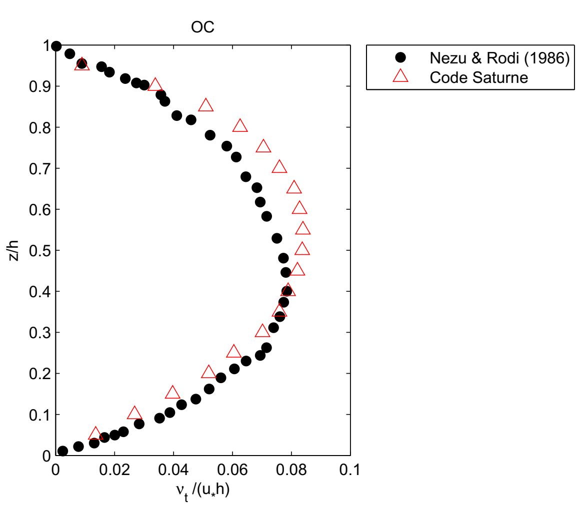

Fig. 18. Comparison between measured and modelled vertical profiles of non-dimensional eddy viscosity for an open channel flow with only currents (OC). Data from Nezu and Rodi (1986).

currents have been proposed (e.g. Christoffersen and Jonsson, 1985; Huang and Mei, 2003).

The turbulence closure model R_{ij}—ϵ has the advantage of solving for the turbulence dissipation ϵ and the Reynolds stresses R_{ij}, without relying on the eddy viscosity assumption. Nevertheless, one may estimate the value of the eddy viscosity a posteriori from the R_{ij}—ϵ model results. In the *Code_Saturne* model, this estimate is obtained with Eq. (10), where k is computed as:

$$k = \frac{1}{2}(R_{xx} + R_{yy} + R_{zz}) \tag{17}$$

These estimates of the turbulence viscosity will be used to determine a parameterisation over the entire depth in relation to external variables. First, the conditions of Nezu and Rodi (1986) experiments, an "only current" (OC) experiment, were considered and presented in Fig. 18. In this figure, z is the elevation from the bottom, h is the water depth, and u_* is the friction velocity. At the bottom and at the (moving) free surface the turbulence viscosity is zero, and it has a parabolic shape over the water depth. These features were well modelled by the *Code_Saturne*, partially showing the effect of the boundary condition (11).

Next, waves were superposed on the current for different values of the wave height and period, as in Umeyama (2005), and the results are shown in Fig. 19. The general shape of the turbulence viscosity profile does not change significantly when compared to the

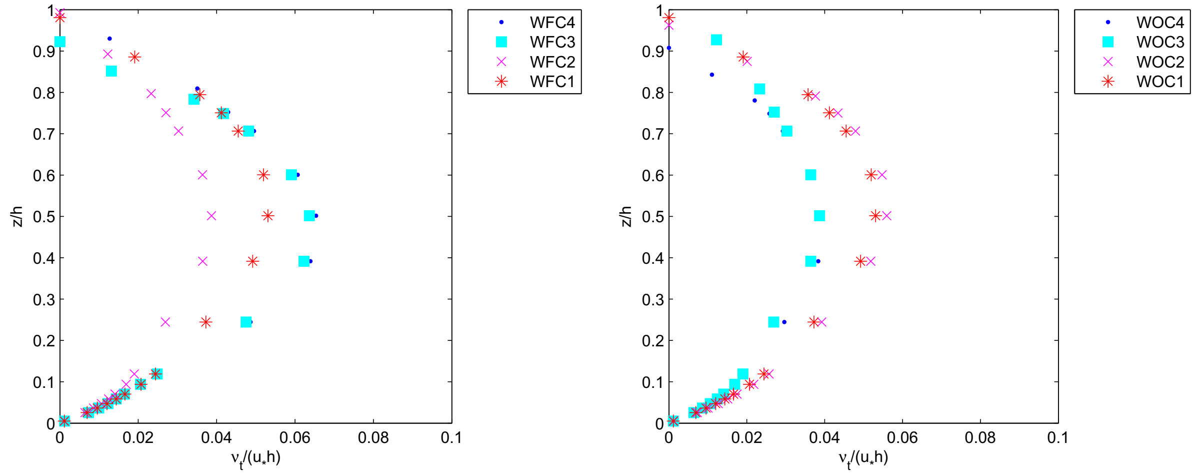

Fig. 19. Vertical profiles of the non-dimensional turbulence viscosity obtained by the *Code_Saturne* using the $R_{ij}-\epsilon$ SSG turbulence closure model for tests with different wave heights and wave periods for "waves following currents " cases (WFC, left panel) and "waves opposing currents " cases (WOC, right panel).

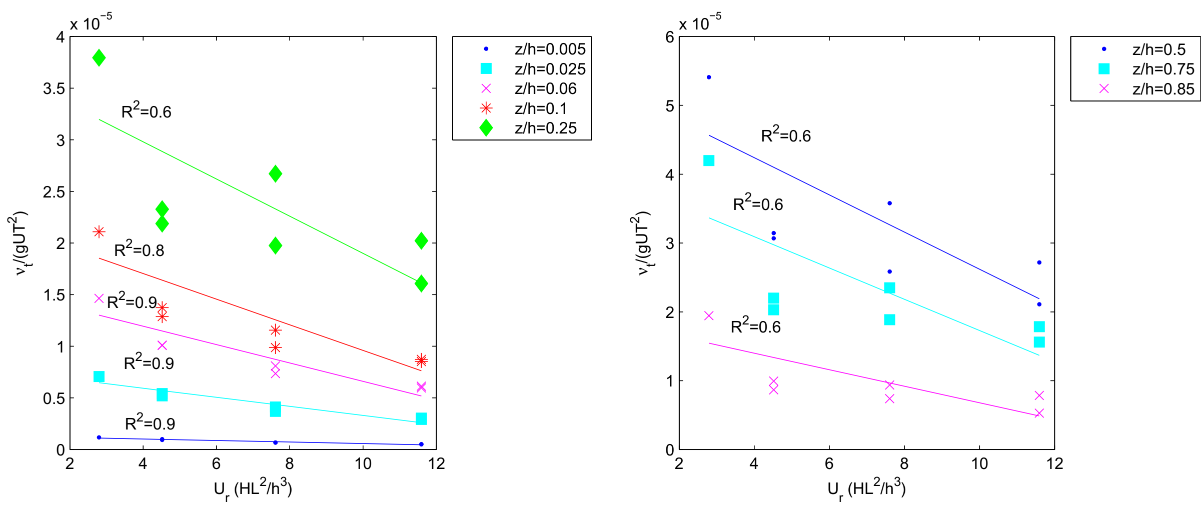

Fig. 20. Variation of the non-dimensional turbulence viscosity $\frac{\nu_t}{gUT^2}$ for each z/h level as a function of the Ursell number $U_r = \frac{HL^2}{h^3}$.

profile of the "only currents" case. Note that Huang and Mei (2003) also considered a parabolic and continuous profile when dealing with smooth bottoms.

The relative similarity of the vertical profiles of the non-dimensional eddy viscosity observed in this set of experiments motivated us to search for a simple parameterisation of the eddy viscosity in combined wave–current flows. This parameterisation could then be used as an input in more simplified numerical models.

We therefore sought out a (simple) dimensionless relation between the turbulence viscosity (ν_t), acceleration due to gravity (g), mean velocity (U), water depth (h), elevation from the bottom (z), wave period (T), wave length (L) and wave height (H). After considering several possible relations, it was found that the non-dimensional eddy viscosity $\frac{\nu_t}{gUT^2}$ at each relative elevation z/h appears to decrease approximately linearly with the so-called Ursell number ($U_r = \frac{HL^2}{h^3}$), as illustrated in Fig. 20. The plotted values correspond to the results of the simulations made with *Code_Saturne* using the Reynolds stress transport model $R_{ij}-\epsilon$.

The trends observed in Fig. 20 can be used to write an expression for the vertical distribution of the nondimensional eddy viscosity as a function of the Ursell number.

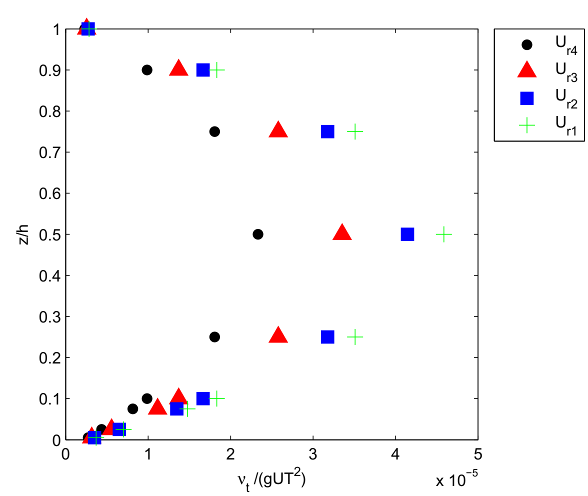

Fig. 21. Vertical distribution of the non-dimensional turbulence viscosity $\frac{\nu_t}{gUT^2}$ in function of non-dimensional water depth z/h for different Ursell numbers ($U_{r1}, U_{r2}, U_{r3}, U_{r4}$) corresponding to the four test wave conditions ($OW1, OW2, OW3, OW4$).

$$\frac{\nu_t}{gUT^2}\left(\frac{z}{h}\right) = \left(10^{-5}U_r - 2\times10^{-4}\right)\left(\frac{z}{h}\right)^2 + \left(-10^{-5}U_r + 2\times10^{-4}\right)\left(\frac{z}{h}\right) + \left(10^{-7}U_r - 2\times10^{-6}\right) \quad (18)$$

Fig. 21 shows the vertical profile of the non-dimensional turbulence viscosity (from (18)) for the wave–current interaction simulations. Here, four different wave conditions ($OW1, OW2, OW3, OW4$), corresponding to four different Ursell numbers ($U_{r1}, U_{r2}, U_{r3}, U_{r4}$), were superposed on a current.

However, we stress that this tentative parameterisation of the eddy viscosity needs to be validated with a more extensive set of data. Once validated, it could be used in simplified models that rely on the eddy viscosity assumption for the turbulence closure scheme.

6. Conclusions

With the aim of studying wave–current interactions in a detailed manner, an existing CFD solver based on the RANS equations (the *Code_Saturne* Archambeau et al., 2004) was applied to model combined wave–current free surface turbulent flows. The wave and current hydrodynamics were thus solved simultaneously at an intra-wave scale. The Arbitrary Lagrangian–Eulerian (ALE) method was used to model the time-varying free surface dynamics.

Four different hydrodynamic conditions were considered: only currents, only waves, waves following currents, and waves opposing currents. Laboratory data from Klopman (1994) and Umeyama (2005) was used to verify the numerical results, with particular attention paid to the vertical profiles of the mean flow velocity, as well as the amplitudes of the horizontal orbital velocity and shear stresses for each of the test cases.

A sensitivity analysis of turbulence closure models in *Code_Saturne* was completed to determine the appropriate model for simulating wave–current interactions. The results were obtained without any modification of the default values of the parameters in the turbulence schemes. A boundary condition for the turbulence dissipation was imposed at the free surface. Celik and Rodi, 1984's expression for the turbulence dissipation at the free surface was used, and it was shown to be essential to reproduce correctly the vertical profile of the Reynolds stresses and turbulence viscosity. In *Code_Saturne*, the second-order Reynolds Stress Transport turbulence model (the $R_{ij}-\epsilon$ SSG version by Speziale et al. (1991)) showed the best performance in the modelling of wave–current interactions when compared to the results obtained with first-order $k-\epsilon$ and $k-\omega$ two-equation models. For these types of flows, the second-order $R_{ij}-\epsilon$ model has the advantage that the Reynolds stresses are solved directly, and the model does not have to make any a priori assumptions about the turbulence viscosity.

As a general conclusion, the various comparisons showed that the model is capable of resolving the vertical structure of the combined flows. The model reproduced well the change in the vertical gradient of the mean horizontal velocity profile caused by the presence of waves following or opposing a mean flow. When waves are superposed in the same direction as the current, there is a significant reduction in the mean horizontal velocity near mid-depth. When waves propagate in the opposite direction of the current, the vertical shear of the horizontal velocity increases. Yang et al. (2006) stated that the wave induced Reynolds stresses, non uniformity of the flow, and secondary currents all contribute to this effect.

When comparing the model results with the data from Umeyama (2005) a good agreement was also obtained. However, no general conclusions could be made concerning the changes in the vertical mean current profiles since the wave height and wave period increases have opposing effects.

It was also observed that the values obtained by linear extrapolation of the mean horizontal velocities estimated from the *Code_Saturne* model are higher than the initially imposed physical roughness (z_0), both for the waves following and waves opposing the currents cases. This effect is a common feature of the wave and current combined environment. This is equivalent to an enhanced roughness which is the so-called apparent roughness.

It is worth to point out that, as a consequence of using a *High Reynolds* number modelling strategy in *Code_Saturne* (i.e. a wall function approach in the vicinity of the bottom (Section 3.2.2)), the model is not able to fully resolve the bottom boundary layer. In order to reach a fully predictive model throughout the whole water column, several options might be considered: one relies on using existing formulas/relationships to predict the apparent roughness from the geometrical roughness and bulk parameters for waves and current (e.g. Perlin and Kit, 2002; Van Rijn, 2007) to be used in a *High Reynolds* number CFD code for the wall function, a second one could be to couple the *High Reynolds* number CFD with a BBL model (such as the one proposed for instance by Fredsøe (1984)), and a third option would be to move to a *Low Reynolds* number modelling strategy with the CFD code. Some of these possibilities will be explored in the near future to improve the present model.

With the data from Umeyama (2005), it was also possible to explore the change in the vertical profile of shear stress for the combined wave–current environment. It was shown that the change of the bed shear stress is important independent of the relative direction of wave propagation. With the superposition of waves and currents a reduction of turbulence stresses is observed not only near the bottom but also throughout the water column.

Since the $R_{ij}-\epsilon$ turbulence closure model offers the advantage of solving for the turbulence dissipation and Reynolds stresses, we also attempted to exploit the numerical results of the second-order scheme to propose a parameterisation of the turbulence viscosity profile as a function of the Ursell number. This type of parameterisation, together with the knowledge gained from this study on the effects of wave–current interactions at local scales, will be used in the forthcoming step of our work to model wave–current interactions at larger scales by using two types of models (one for the mean flow and one for the waves), which will then have then to be coupled properly.

Acknowledgements

Maria João Teles would like to acknowledge the support of a PhD grant (SFRH/BD/61269/2009) from FCT (Fundação para a Ciência e Tecnologia), Portugal. The authors would also like to acknowledge the *Code_Saturne* development team for the support, the anonymous reviewers for their valuable suggestions and comments and Marissa Yates-Michelin for reviewing the text.

References

Apsley, D., Hu, W., 2003. CFD simulation of two- and three-dimensional free-surface flow. International Journal for Numerical Methods in Fluids 42, 465–491.

Archambeau, F., Guimet, V., Bastin, G., 1999. Application du prototype de module ALE du Solveur Commun à des cas de surface libre. Technical report EDF HE-41/99/054/A, EDF Research and Development, Chatou, France (in French).

Archambeau, F., Méchitoua, N., Sakiz, M., 2004. CodeSaturne: a finite volume method for the computation of turbulent incompressible flows – industrial applications. International Journal on Finite Volumes 1 (1), 1–62.

Celik, I., Rodi, W., 1984. Simulation of free surface effects in turbulent channel flows. Physicochemical Hydrodynamics 5, 217–227.

Christoffersen, J.B., Jonsson, I.G., 1985. Bed friction and dissipation in a combined current and wave motion. Ocean Engineering 12, 387–423.

Cozzi, O., 2010. Free surface flow simulation: correcting and benchmarking the ALE method in Code_Saturne. M.Phil. Thesis, University of Manchester, UK.

Dean, R.G., Dalrymple, R.A., 1991. Water wave mechanics for engineers and scientists. Advanced Series Ocean Engineering, vol. 2. World Scientific.
Dingemans, M.W., van Kester, J.A.T.M.V., Radde, A.C., Uittenbogaard, R.E., 1996. The effect of the CL-vortex force in 3D wave–current interaction. In: Proc. 25th International Conference on Coastal Engineering (ICCE'1996), Orlando, FL, USA, pp. 4821–4832.
Dore, B.D., 1978. Some effects of the air–water interface on gravity waves. Geophysics Astrophysics Fluid Dynamics 10, 215–230.
Fredsøe, J., 1984. Turbulent boundary layer in wave–current motion. Journal of Hydraulic Engineering, ASCE 110, 1103–1120.
Fredsøe, J., Andersen, K.H., Mutlu Sumer, B., 1999. Wave plus currents over a ripple-covered bed. Coastal Engineering 38, 177–221.
Grant, W.D., Madsen, O.S., 1979. Combined wave and current interaction with a rough bottom. Journal of Geophysical Research 84 (C4), 1797–1808.
Groeneweg, J., Battjes, J.A., 2003. Three dimensional wave effects on a steady current. Journal of Fluid Mechanics 478, 325–343.
Groeneweg, J., Klopman, G., 1998. Changes of the mean velocity profiles in the combined wave–current motion described in a GLM formulation. Journal of Fluid Mechanics 370, 271–296.
Guimet, V., Laurence, D., 2002. A linearised turbulent production in the $k-\epsilon$ model for engineering applications. In: Rodi, W., Fueyo Edts, N. (Eds.), Fifth International Symposium on Engineering Turbulence Modelling and Measurements. Elsevier, Mallorca, Spain.
Holmedal, L.E., Myrhaug, D., Rue, H., 2003. The sea bed boundary layer under random waves plus current. Continental Shelf Research 23 (7), 717–750.
Holmedal, L.E., Myrhaug, D., Rue, H., 2009. Wave-induced steady streaming, mass transport and net sediment transport in rough turbulent ocean bottom boundary layers. Continental Shelf Research 29, 911–926.
Houwman, K.T., van Rijn, L.C., 1999. Flow resistance in the coastal zone. Coastal Engineering 38, 261–273.
Huang, Z., Mei, C.C., 2003. Effects of surface waves on a turbulent current over a smooth or rough seabed. Journal of Fluid Mechanics 497, 253–287.
Kemp, P.H., Simons, R.R., 1982. The interaction between waves and a turbulent current: waves propagating with the current. Journal of Fluid Mechanics 116, 227–250.
Kemp, P.H., Simons, R.R., 1983. The interaction between waves and a turbulent current: waves propagating against the current. Journal of Fluid Mechanics 130, 73–89.
Klopman, G., 1994. Vertical structure of the flow due to waves and currents: laser-Doppler flow measurements for waves following or opposing a current. Progress Report H840.30 Part II, Delft Hydraulics, Delft.
Klopman, G., 1997. Secondary circulation of the flow due to waves and current: laser-Doppler flow measurements for waves following or opposing a current. Tech. Rep., Delft Hydraulics Z2249, Delft.
Longuet-Higgins, M.S., 1953. Mass transport in water waves. Philosophical Transactions of the Royal Society A 245, 535–581.
Lundgren, H., 1972. Turbulent currents in the presence of waves. In: Proc. 13th International Conference on Coastal Engineering (ICCE'1972), Vancouver, Canada, pp. 623–634.
Menter, F.R., 1994. Two-equation eddy-viscosity turbulence models for engineering applications. AIAA Journal 32 (8), 1598–1605.
Muzaferija, S., Peric, M., 1997. Computation of free-surface flows using the finite-volume method and moving grids. Numerical Heat Transfer, Part B 32, 369–384.
Nezu, I., Nakagawa, H., 1993. Turbulence in Open-Channel Flows. A.A. Balkema, CRC Press, Rotterdam.
Nezu, I., Rodi, W., 1986. Open channel flow measurements with a laser Doppler anemometer. Journal of Hydraulic Engineering 112 (5), 335–355.
Nielsen, P., You, Z., 1996. Eulerian mean velocities under non-breaking waves on horizontal bottoms. In: Proc. 25th International Conference on Coastal Engineering (ICCE'1996), Orlando, FL, USA, pp. 4066–4078.
Olabarrieta, M., Medina, R., Castanedo, S., 2010. Effects of wave–current interaction on the current profile. Coastal Engineering 57 (7), 643–655.
Perlin, A., Kit, E., 2002. Roughness in wave–current flow: implication for coastal studies. Journal of Hydraulic Engineering 128 (8), 729–741.
Song, T., 1994. Velocity and turbulence distribution in non-uniform and unsteady open-channel flow. PhD Thesis, Ecole Polytechnique Fédérale de Lausanne, Switzerland.
Soulsby, R., Hamm, L., Klopman, G., Myrhaug, D., Simons, R., Thomas, G., 1993. Wave current interaction within and outside the bottom boundary layer. Coastal Engineering 21, 41–69.
Speziale, C.G., Sarkar, S., Gatski, T.B., 1991. Modeling the pressure-strain correlation of turbulence: an invariant dynamical systems approach. Journal of Fluid Mechanics 227, 245–272.
Teles, M.J., Benoit, M., Pires-Silva, A.A., 2013. Modelling combined wave–current flows using a RANS CFD solver with emphasis on the effect of the turbulence closure model. Advances in Hydroinformatics, Springer, in press.
Umeyama, M., 2005. Reynolds stresses and velocity distributions in a wave–currents coexisting environment. Journal of Waterway, Port, Coastal and Ocean Engineering 131 (5), 203–212.
Van Rijn, L., 2007. Unified view of sediment transport by currents and waves. I: Initiation of motion, bed roughness, and bed-load transport. Journal of Hydraulic Engineering 133 (6), 649–667.
Yang, S., Tan, S.-K., Lim, S.-Y., Zhang, S.-F., 2006. Velocity distribution in combined wave–current flows. Advances in Water Resources 29, 1196–1208.
You, Z., 1996. The effect of wave-induced stress on current profiles. Ocean Engineering 23, 619–628.